

Proton beam behavior in a parallel configured MRI-proton therapy hybrid: Effects of time-varying gradient magnetic fields

D. M. Santos^{a)}

Department of Medical Physics, Cross Cancer Institute, 11560 University Avenue, AB T6G 1Z2, Canada

K. Wachowicz

Department of Medical Physics, Cross Cancer Institute, 11560 University Avenue, AB T6G 1Z2, Canada

Department of Oncology, Medical Physics Division, University of Alberta, 11560 University Avenue, Edmonton, AB T6G 1Z2, Canada

B. Burke

Department of Oncology, Medical Physics Division, University of Alberta, 11560 University Avenue, Edmonton, AB T6G 1Z2, Canada

B. G. Fallone

Department of Medical Physics, Cross Cancer Institute, 11560 University Avenue, AB T6G 1Z2, Canada

Department of Oncology, Medical Physics Division, University of Alberta, 11560 University Avenue, Edmonton, AB T6G 1Z2, Canada

Department of Physics, University of Alberta, 11322 – 89 Avenue, Edmonton, AB T6G 2G7, Canada

MagnetTx Oncology Solutions, Ltd., PO Box 52112, Edmonton, AB, Canada

(Received 14 June 2018; revised 18 November 2018; accepted for publication 19 November 2018;
published 18 December 2018)

Purpose: Real-time magnetic resonance (MR) guidance is of interest to various groups globally because the superior soft tissue contrast MR images offer over other x-ray-based imaging modalities. Because of the precision required in proton therapy, proton therapy treatments rely heavily on image guidance. Integrating a magnetic resonance imaging (MRI) into a proton therapy treatment is a challenge. The charged particles (protons) used in proton therapy experience magnetic forces when travelling through the MRI magnetic fields. Given that it is desired that proton beams can be delivered with submillimeter accuracy, it is important that all potential sources of beam displacement are well modeled and understood. This study investigated the behavior of monoenergetic proton beams in the presence of a simulated set of realistic three-dimensional (3D) vector magnetic gradient fields required for spatial localization during imaging. This deflecting source has not been previously investigated.

Methods: Three-dimensional magnetic vector fields from a superconducting 0.5 T open bore MRI magnet model (previously developed in-house) and 3D magnetic fields from an in-house gradient coil model were applied to two types of computer simulations. In all simulations, monoenergetic proton pencil beams (from 80 to 250 MeV) were used. The initial directions of proton beams were varied. In all simulations, the orientation of the \mathbf{B}_0 field coincided with the positive z-axis in the simulation geometry. The first type of simulation is based on an analytic magnetic force equation (analytic simulations) while the second type is a full Monte Carlo (MC) simulation. The analytic simulations were limited to propagating the proton beams in vacuum but could be rapidly calculated in a desktop computer while the MC simulations were calculated in a cluster computer. The proton beam locations and dose profiles at the central plane ($z = 0$ cm) with or without magnetic fields were extracted and used to quantify the effect of the presence of the different magnetic fields on the proton beam.

Results: The analytic simulations agree with MC results within 0.025 mm, thus acting as the verification of MC calculations. The presence of the \mathbf{B}_0 field caused the beam to follow a helical trajectory which resulted in angular offsets of 4.9°, 3.6°, and 2.8° for the 80, 150, and 250 MeV, respectively. Magnetic field deflections caused by a rapid MRI sequence (bSSFP, with maximum gradient strength of 40 mT/m) show a pattern of distortion which remained spatially invariant in the MR's field of view. For the 80 MeV beam, this pattern shows a maximum ranged in the y direction of 1.5 mm. The presence of the \mathbf{B}_0 field during the bSSFP simulations adds the same beam rotation to the observed during the \mathbf{B}_0 only simulations.

Conclusion: This investigation reveals that time-varying gradient magnetic fields required for image generation can cause a small spread in the proton beams used in the study which are independent of the effects arising from the \mathbf{B}_0 field. Further, studies where clinical beam kernels were convolved with this spread show that these magnetic fields are expected to have an insignificant impact on the beam's entrance dose. © 2018 American Association of Physicists in Medicine [<https://doi.org/10.1002/mp.13309>]

Key words: magnetic fields, MR guided, proton, proton therapy, real time

1. INTRODUCTION

Real-time image guidance is a major interest in current radiation therapy (radiotherapy). It uses information from imaging sources to shape the radiation beam closer to the tumor's three-dimensional (3D) morphology. Therefore, it may reduce dose delivered to the patient's healthy tissue to further diminish unwanted side effects from the cancer treatment. The integration of an MR imager with a radiotherapy unit has been proposed and is being worked on by various groups globally.^{1–4} In MR-guided radiotherapy, the MR imager is used because it offers real-time imaging with superior soft tissue contrast without the resulting deposited dose from the other x-ray-based imaging modalities. The linear accelerator (linac) is a reliable unit for producing and delivering x rays. Solutions to various challenges to the linac-MR integration, such as electron gun shield and design,^{5,6} decoupling between the linac and MR imager,^{7–9} RF shielding,^{10,11} and the magnet designed,^{2,12} have been published.

Unlike conventional radiotherapy, proton therapy uses proton beams instead of x rays to treat cancer. Proton beams have a finite range in tissue. In addition, they deposit the majority of their dose near the end of their track; therefore, it has the potential to further reduce the irradiated volume of healthy tissue during treatment. Because of this increased precision, image guidance plays an important role in this modality. MR-guided proton therapy, like the linac-MR system, would use the MR imager's superior soft tissue contrast while taking advantage of the increased precision offered by proton beams. As these beams are composed of charged particles, the effect of the magnetic resonance imaging's (MRI) magnetic fields on the proton trajectories and resulting dose distributions need to be explored. While fewer than MR-guided x-ray radiotherapy, there have been publications that explore the feasibility of an MR-guided proton system.^{13–21} Recently, there have been some publications that explore numerical algorithms to predict proton trajectory and dose deposition in magnetic field without utilizing time-consuming Monte Carlo techniques.^{22–24} In contrast, this work focuses not on the algorithm, but on the characterization of beam distortions due to the time-varying magnetic fields produced by the MRI's gradient coils which are essential for image generation. Collectively, these magnetic fields will be referred to as the gradient fields. Since proton therapy is ideally targeted with submillimeter accuracy, it is essential to consider all sources of deflection and characterize their behavior. Although there are sources of magnetic fields outside of the MRI system such as the XY scanning magnets in the nozzle and the stirring magnets used to deliver the synchrotron/cyclotron beam line to the nozzle, these external magnetic field sources are beyond the scope of the study. The focus of this study is specifically on the effects of the magnet fields from the MRI magnet and gradient coils on the proton beam. Imaging gradients generate magnetic fields within the central field of view (FOV) on the order of several mT (orders of magnitude smaller than the primary magnetic field²⁵). As such, one can expect substantially less effect. However, the

strongest fields generated by the gradient coils are not in the central FOV of the imaging system, but rather get stronger as you move away from isocenter and toward the conductive elements that create the fields, as a consequence of the $1/r^2$ relationship in the Biot–Savart law. Moreover, while the coils are designed to maintain a linearly varying field in the \mathbf{B}_0 direction within the central imaging FOV, nonaxial field components can dominate outside this central region. As such, when dealing with such a complex field distribution, nothing short of a full 3D field simulation can yield reliable results. This is the first report detailing the effects of these gradient fields in an MRI proton therapy hybrid. The objective of this work is to explore the degree and nature of the changes in proton trajectories resulting from the 3D magnetic vector fields created by a physically realistic set of gradient coils and the potential extent of the effect on a treatment beam. To achieve this goal, this study uses computer simulations.

2. MATERIALS AND METHODS

This work investigates the impact of two different types of magnetic fields (static and the time-varying fields) produced by an MRI system on a therapeutic proton beam. Specifically, it examines the effects of both the main magnetic field (\mathbf{B}_0) and the time-varying gradient fields. For simplicity only the proton beam is simulated; the physical components of the proton system were not included in the simulations.

2.A. The \mathbf{B}_0 field

The MR imager used in this study is similar to the MRI used by Fallone et al. in the Alberta linac-MR design.^{12,26–28} This work assumes that enough space is available for the compact scanning magnets²⁹ needed to deflect the proton beam in a scanning proton pencil beam system (PBS). The magnetic shield shown as the blue structures in the Fig. 1(b) was originally used to passively shield the MLC assembly of the linac-MR from the MRI's magnetic fields. However, these shields can aid in magnetically decoupling the PBS's scanning magnets from the MRI, although a redesign of this magnetic shield may be required for further development of an integrated proton-MR system. In these simulations, the MR system is integrated with a proton PBS in a parallel configuration (also referred to as in-line¹⁵) in place of a linac. This aligns the direction of the proton beam with the \mathbf{B}_0 field. The effect of the gradient fields on the proton trajectories was studied both with and without the presence of the \mathbf{B}_0 field. The MRI's \mathbf{B}_0 fields were calculated using finite element analysis (FEM), based on a 3D model of the linac-MR imager, using the OPERA-3d/TOSCA software (Cobham Technical Services, Kidlington, UK).^{12,26,28} The full 3D vector components of the magnetic fields were extracted from the 3D model and placed into a rectilinear grid covering a volume defined by a width of 60 cm for the x and y directions, and 150 cm for z (starting from -130 cm, the point where the proton beam is introduced, and extending 20 cm past the isocenter). Figure 1(a) shows the magnitude and direction of

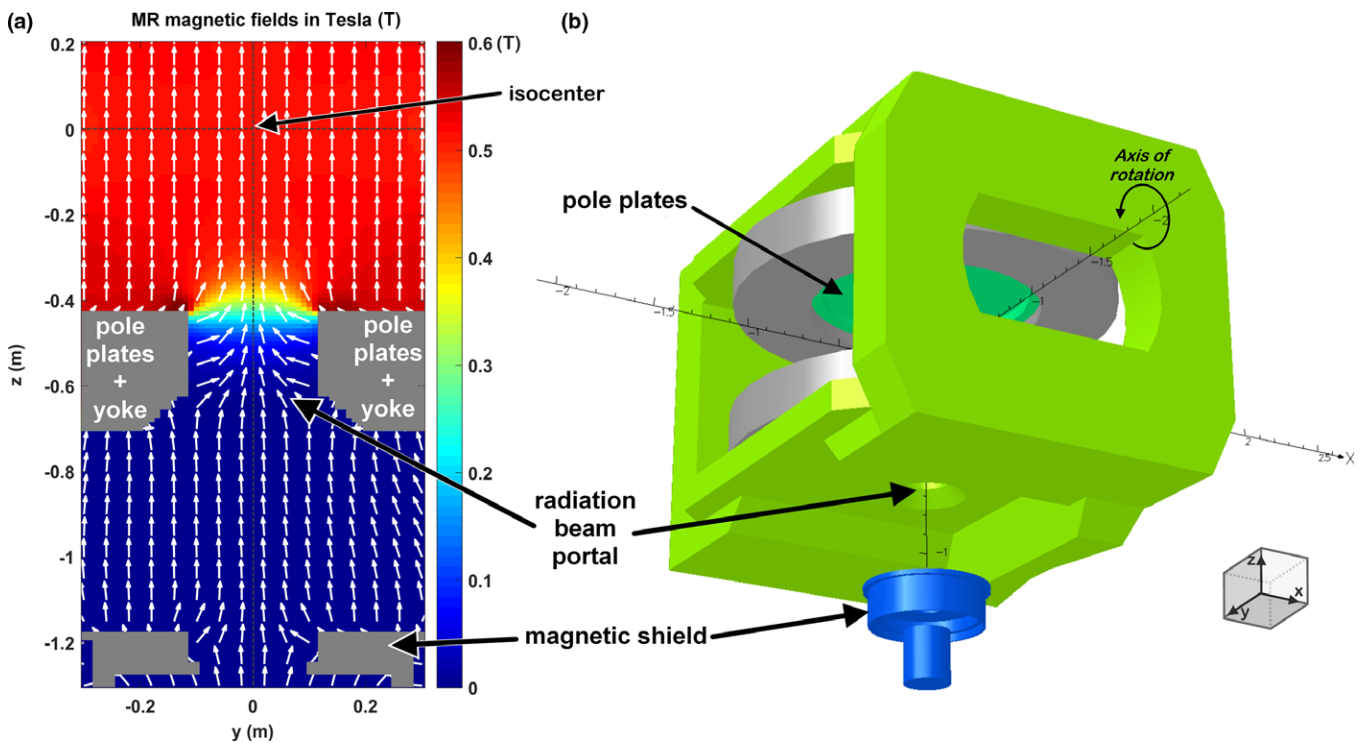


Fig. 1. (a) A cross-sectional cutout of the magnetic fields (T) along the central yz plane of the MR magnet. The arrows (white) show the field direction while the color scale shows its magnitude in Tesla. (b) This three-dimensional model of the magnet is used to generate the \mathbf{B}_0 magnetic fields shown in (a). Both the MR magnet and proton nozzle would rotate in a similar fashion to the Alberta linac-MR system. Although a redesign may be required, the magnetic shield (originally used to magnetically shield the MLC assembly) can be used to passively shield the MRI from the magnetic fields generated by the XY scanning magnets inside the proton nozzle. [Color figure can be viewed at wileyonlinelibrary.com]

the magnetic fields from the linac-MR imager^{26–28} from its central yz-plane and shows that this magnet was designed to have minimal magnetic field strengths from the radiation beam portal to the radiation (proton) source. The space between grid points was 1 cm in the x, y, and z directions. The magnetic field map data were written into an input file. The direction of the \mathbf{B}_0 field was defined as being along the positive z direction as seen in Fig. 2.

For all the simulations presented in this work, proton beams in a proton PBS are further approximated by monoenergetic, infinitely thin beams. This monoenergetic approximation is made since the energy spread is expected to be small (~0.2%).³⁰ The infinitely thin proton beam is used since this work only looked at the beam's central location; however, beams of a proton PBS have circular spot sizes with an approximately Gaussian density distribution.³¹ Its width can be described by the standard deviations σ which may vary from 1 to 5 mm.^{32,33} In the clinic, the direction of a scanning proton beam is controlled through a set of X and Y scanning magnets.^{29,34} However, for this work, the proton beam direction will be described through two angles, θ and ϕ , as a simplification. θ is the angle between the beam direction and the positive z-axis, and ϕ is the angle between the beam direction and the positive x-axis (illustrated in Fig. 2). The source-to-axis distance (SAD) of proton PBS is generally around 200–300 cm.³⁵ However, this study used magnet design of the Alberta linac-MR with the proton nozzle in place of the linac

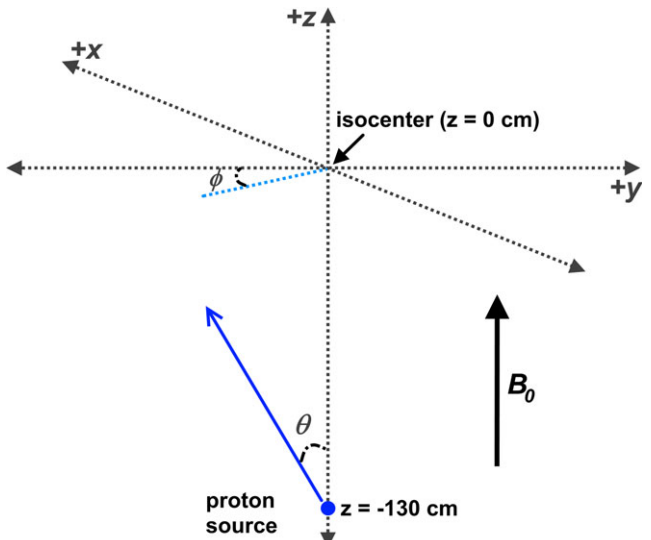


Fig. 2. Simulation geometry setup describing the initial location and direction of the proton beams source used for the simulations. The direction of the \mathbf{B}_0 field coincides with the z-axis in the simulations. [Color figure can be viewed at wileyonlinelibrary.com]

head. This design places the proton source closer to the magnet isocenter ($z = 0$ cm plane) at 130 cm SAD. Therefore, a stronger x- and y-rastering magnetic fields would be required to create the expected 30 cm diameter field at the isocenter. This shorter SAD was maintained in an attempt to make the

integrated proton and MR system compact. An additional benefit for using the shorter SAD is the reduction in clinical pencil beam's spot size, where the lower energy beams receive the most reduction.³²

Both analytical and Monte Carlo (MC) simulations are used in this investigation. First, analytic equations are utilized to calculate the proton trajectory along its path in the presence of magnetic fields in a similar fashion to recently published works.^{22,23,36,37} Since the interest of this work is to track the beam along its path in vacuum, energy loss need not be incorporated into these simulations in contrast to the numerical methods proposed by those published works. A vacuum column as shown in Fig. 3 is placed between the source and the magnet isocenter to reduce the scattering that would occur because of the 130 cm air gap. Three proton energies (80, 150, and 250 MeV) are used during the simulations. For both the analytical and MC simulations, the range of ϕ was limited from 0° to 90° in steps of 45° to take advantage of the symmetry in the MR's \mathbf{B}_0 fields while θ which was restricted by a 24 cm-diameter radiation beam portal that run through the yoke (see Fig. 1) and the gradient coil (see Fig. 6) was varied from 0° to 6.8° in steps of 1° . This beam portal in Fig. 1 allows the proton beam to reach the magnet's FOV unimpeded. The vacuum column (Fig. 3) protrudes into

the magnet by an additional 10 cm beyond the gradient coil; therefore, a cap with a radius of 13.5 cm was added to all the simulations to account for the lateral distance that the beam would travel inside this 10 cm region. For each pair of ϕ and θ used, simulations, with and without the magnetic fields present, are performed.

$$\mathbf{F}_m = q\mathbf{v} \times \mathbf{B} \quad (1)$$

$$v = c \sqrt{1 - \left(\frac{K}{E_0} + 1\right)^{-2}} \quad (2)$$

The analytic simulations are implemented through an in-house code written in Matlab (Mathworks, Massachusetts, USA). These simulations calculate the magnetic force, \mathbf{F}_m in Eq. (1), at each proton location by interpolating the magnetic field value for the proton's location from the 3D magnetic field map \mathbf{B} . \mathbf{B} can include \mathbf{B}_0 with or without gradient fields, and covers a rectangular region that extends from -30 to 30 cm in x and y directions and from -130 to 20 cm in the z direction as per Fig. 3. In Eq. (1), q is the proton charge in Coulombs, and v is the proton's relativistic velocity calculated from Eq. (2). In Eq. (2), c is the speed of light; K is the

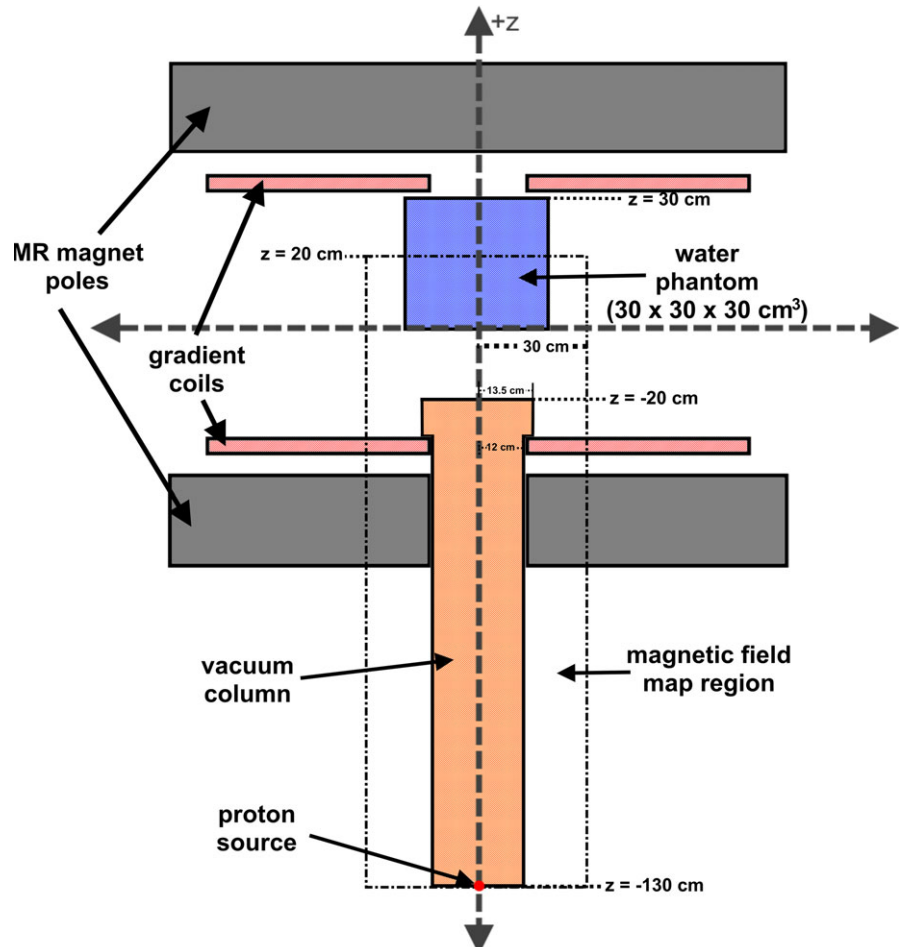


FIG. 3. A cross section along the z -axis of the geometric setup for all the simulations. [Color figure can be viewed at wileyonlinelibrary.com]

initial kinetic energy of the proton; and E_0 is the proton rest energy. \mathbf{F}_m is applied to the relativistic proton to calculate the distance and direction this proton travelled during a user-defined time step Δt , which is set to 0.01 ns. The proton's position is updated by adding this distance to its current position. The calculated direction replaces the proton's previous direction for the new time $t + \Delta t$. This entire procedure is repeated at the new position until the proton exits the defined magnetic field map region from Fig. 3. After each time step, the proton position is recorded to an output file. The proton positions for cases with and without the \mathbf{B} field are determined. A flowchart of the particle tracking simulation process is illustrated in Fig. 4.

The MC simulations are used to determine the beam's surface dose on a $30 \times 30 \times 30$ cm³ water phantom. This phantom is surrounded by air and placed in the magnet according to Fig. 3. The MC simulations are also used to benchmark the proton locations (not the dose) determined by the analytic simulations described above.

All MC simulations are performed in a cluster computer operated and supported by WestGrid which is one of four regional high-performance computing (HPC) consortia in Canada. The cluster used contains a combination of Intel™ Xeon E5450 quad-core CPUs running at 3 GHz and Intel™ Xeon X5650 six-core CPUs running at 2.66 GHz. The total number of cores available for use is 9600 cores. The MC simulations are performed using the GEometry ANd Tracking

(GEANT4) MC toolkit³⁸ (GEANT4 ver 9.5.p02). Magnetic fields are implemented in the MC simulations by following the steps in the *Purging Magnet* example in the GEANT4 package. The delta one step parameter in the G4FieldManager object is decreased from its default value of 5.0×10^{-3} mm to 5.0×10^{-4} mm to decrease the positional error in each of the integration step. Other magnetic field settings are kept at default for all the MC simulations. The 3D magnetic field map is read from the input file described earlier, and trilinear interpolation is again used to calculate the magnetic fields for arbitrary locations. The MC simulations are run with the following options: G4EmStandardPhysics_option3 for the electromagnetic physics interactions; G4DecayPhysics for the particle decay; and G4NeutronCrossSectionXS and HadronPhysicsQGSP_BIC for hadronic processes. The range cuts for gammas, electron and positrons, and proton are set to 0.025 mm, 0.025 mm, and 0.015 mm, respectively. The maximum step length for the entire simulation is limited to 10 mm.

All MC simulations use monoenergetic pencil beams. The source of these beams is placed at $z = -130$ cm (Fig. 3). The magnet poles in Fig. 3 are also included in the simulations. A $30 \times 30 \times 30$ cm³ water phantom is used and is divided into $0.025 \times 0.025 \times 0.025$ mm³ voxels, in which the deposited dose is scored. Four MC simulations are run for each θ and ϕ combination. The first two simulations, performed for benchmarking the analytic simulations, use a

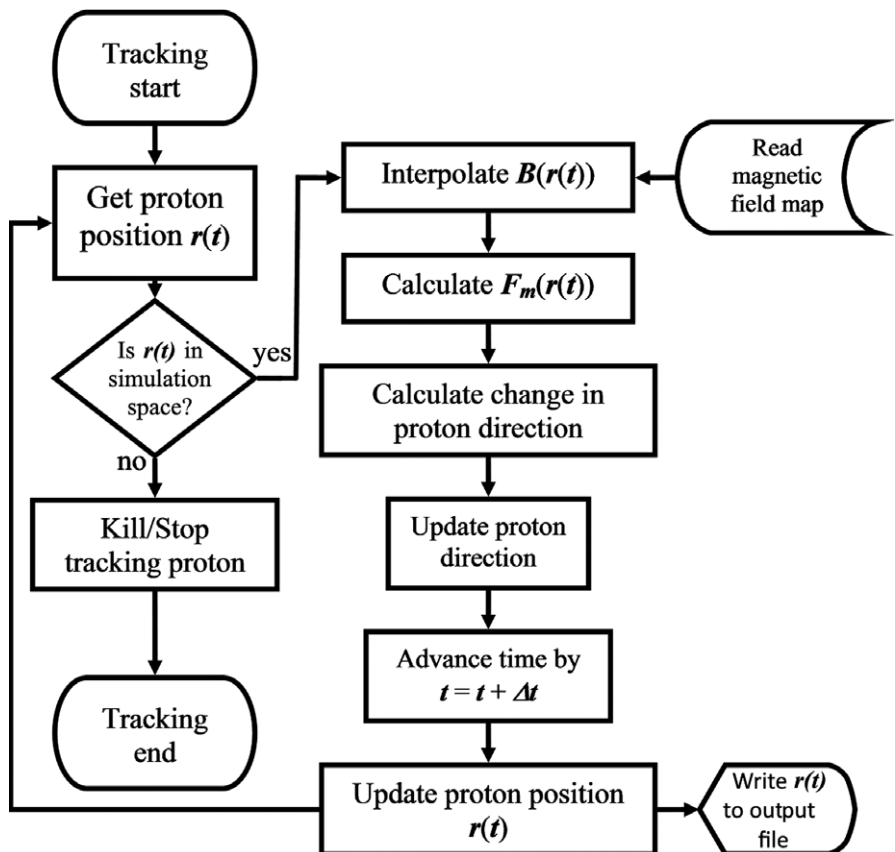


FIG. 4. This flowchart describes the algorithm used in the analytic simulations

vacuum background material with and without the \mathbf{B}_0 field. The location of the beam as it enters the phantom is extracted and is compared to the analytic results. The other two MC simulations replaced the vacuum with air with and without the \mathbf{B}_0 field. From these simulations, the beam's entrance location and two-dimensional (2D) surface dose profiles are extracted and used to quantify the effect of the \mathbf{B}_0 field on the beam.

2.B. The gradient fields

Other sources of magnetic fields that originate from the MR imager are generated by the three gradient coils: \mathbf{G}_x , \mathbf{G}_y , and \mathbf{G}_z . During the imaging process, these coils produce time-varying magnetic fields (gradient fields). This part of the investigation studies the effects of these gradient fields

from a rapid MRI imaging sequence on mono energetic proton pencil beams. For this work, a balanced steady-state free precession³⁹ (bSSFP) sequence, represented in Figs. 5(a) and 5(b), is used as an example of a rapid, real-time MRI imaging sequence. This sequence is chosen because of its intensive gradient playout; there is little-to-no time when a gradient pulse is not being executed. In this way, the sequence can be considered as a worst-case scenario. Two versions of this sequence are investigated: the sequence in Fig. 5(a) has a maximum gradient strength of 20 mT/m (bSSFP20) and the other in Fig. 5(b) has a maximum of 40 mT/m (bSSFP40). The three waveforms displayed for each sequence in Fig. 5 represent the variation in gradient strength over one repetition time (2.25 ms for this implementation) for the three gradient coils. The \mathbf{G}_z coil is assigned the function of slice selection, which is reasonable given that slices must be defined in the

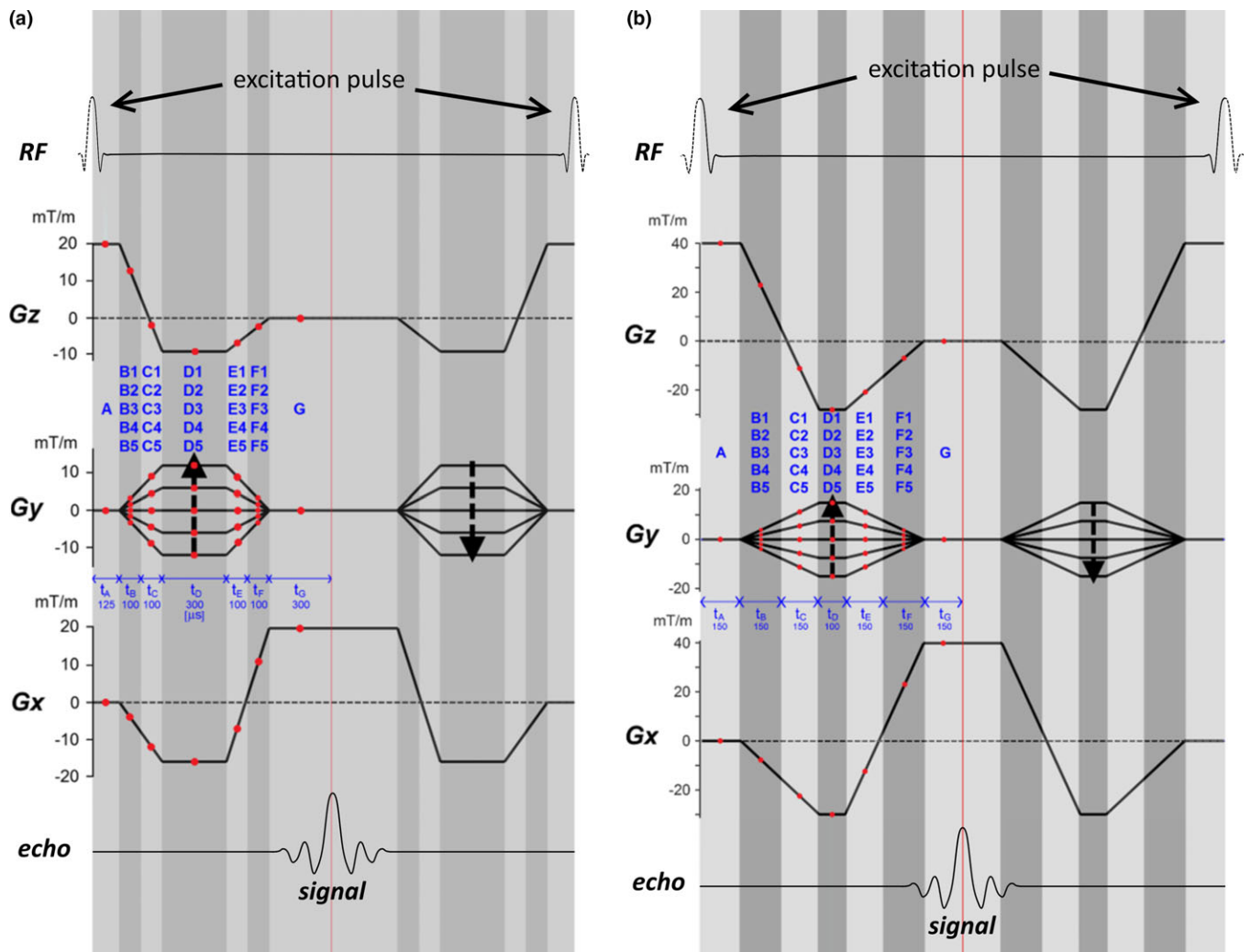


Fig. 5. Schematic diagrams of the two bSSFP sequences used to investigate the effect of the gradient coils' magnetic fields on the proton beam: the sequence in (a) have a maximum field strength of 20 mT/m (bSSFP20) and the sequence in (b) have a maximum field strength of 40 mT/m (bSSFP40). For each sequence, the three plots represent the variation in each of the three gradient coil strengths over one complete repetition time (2.25 ms for this implementation). The dark and light gray shading shows how the sequence is divided into smaller segments that were used in both the analytic simulations and Monte Carlo simulations. Note that due to symmetry, only the sections marked A through G need to be considered. The variations due to phase encoding were represented by five subdivisions, seen in sections B, C, D, E, and F. The red dots represent the mean gradient strengths in each section. Segment A corresponds to slice selection, and segment G corresponds to the readout (acquisition) stage of the sequence. [Color figure can be viewed at wileyonlinelibrary.com]

z-axis to create images in the beam's eye view. For spatial encoding in-plane, the G_x and G_y coils are assigned the functions of read encoding and phase encoding, respectively. This sample sequence is designed to be capable of 2 mm in-plane resolution, with a frame rate of three per second or more when the phase-encoding FOV is less than 300 mm. In order to visualize the distorting effect of the gradient fields on the proton beam, the sequence is segmented into bins, where the gradient strength of each coil is assumed to be constant. As presented in Figs. 5(a) and 5(b), A is the slice selection segment, G represents the readout stage. Lastly, segments B, C, D, E, and F are different parts of the phase-encoding steps of the sequence though all of these segments (B–F) also contained prep and rewind lobes associated with slice selection and readout. Each ramp in the phase-encoding steps is subdivided into two bins so that the change in trajectory during the

ramp could be tracked. The gradient strength during these ramp regions is the average within the bin.

One of the potential gradient coil designs,^{1,28} shown in Fig. 6, is used to generate a realistic 3D vector model of the magnetic fields produced by these devices. These coil patterns are generated using in-house software based on the technique described by Lemdiasov et al. and Poole et al., which utilizes a boundary-element methodology.^{40,41} Two annular surfaces with an inner and outer diameter of 24 and 100 cm and a separation of 60 cm are first defined in a FEM software package (COMSOL™ Multiphysics), which is then used to generate a triangular mesh with node spacing on the order of 3 cm. This mesh is then exported to Matlab which is then used to optimize the current distribution pattern on the two surfaces. The current distribution is optimized subject to the production of a maximally linear B_z distribution in either

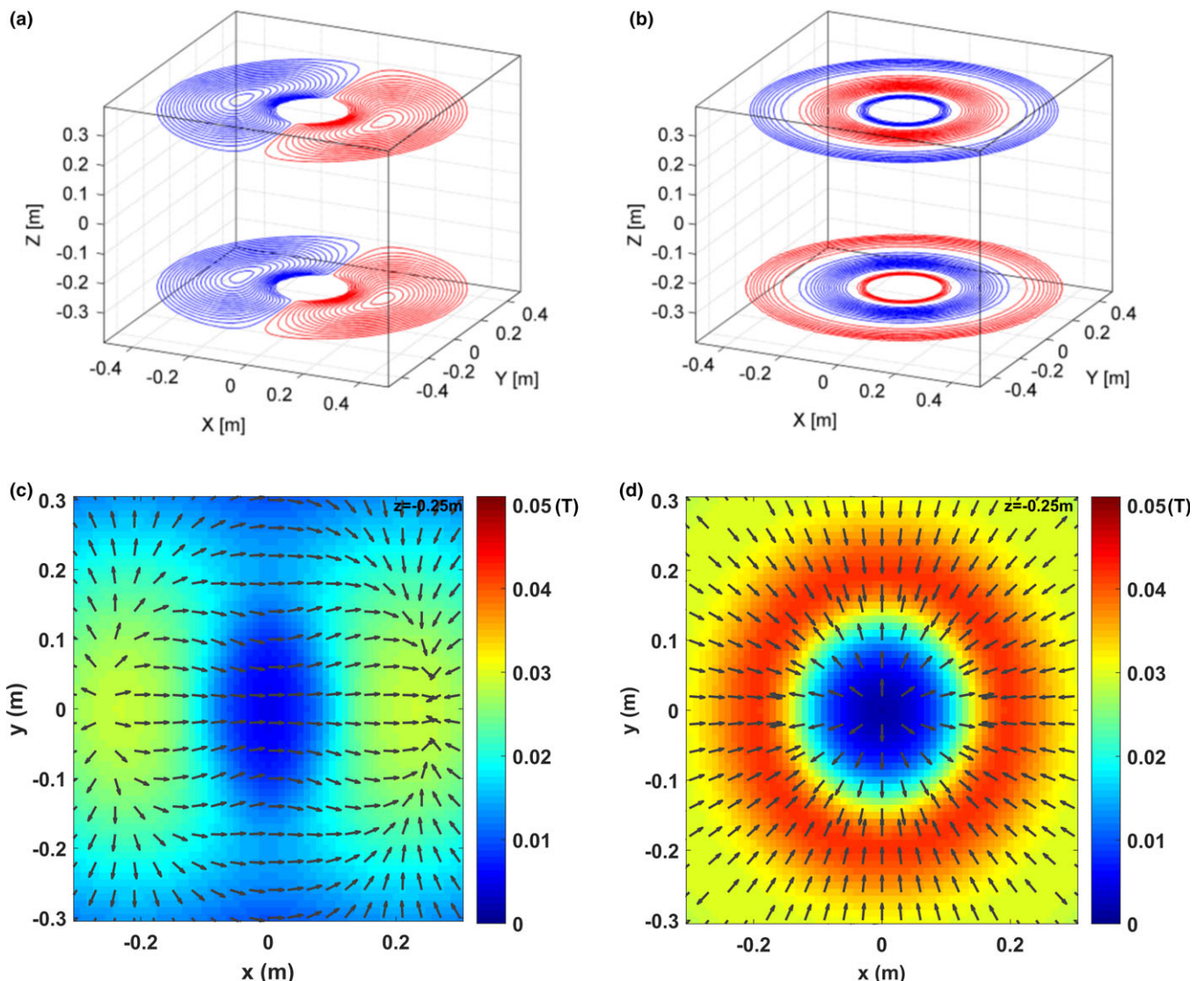


Fig. 6. The three-dimensional model of the (a) G_x gradient coils design and (b) G_z gradient coil design. Both figures show the currents in the coil and the 24-cm hole (radiation beam portal) on the coil design which allow for an unimpeded proton beam passage to the center of the MR magnet. The blue and red coils show opposite current flow in both (a) and (b). The magnetic field (in Tesla) at $z = 0.25\text{ m}$ when the G_x and G_z coils are turned on at full strength (40 mT/m) are shown in the field maps (c) and (d), respectively. The colorscale shows the field strength while the arrows show the in plane field direction. The G_y gradient coil will have an identical design as in (a), except for a 90-degree rotation about the z -axis. [Color figure can be viewed at wileyonlinelibrary.com]

x or z (over a region consisting of a 40 cm diameter sphere centered on the MR's isocenter), subject to the constraints of minimal inductance and minimal resistive power losses. Figures 6(a) and 6(b) show only the G_x and G_z coils; however, the G_y coils have an identical design as in Fig. 6(a), except for a 90° rotation about the z-axis. The resulting current distributions are discretized to individual current pathways. Given a constant current for all these discrete pathways, the Biot-Savart law is used to calculate the resulting magnetic vector field for each gradient coil over a rectilinear grid covering a region defined by -30 to 30 cm in the x and y direction and -130 to 20 cm in the z direction seen in Fig. 3. The grid spacing for this field distribution is 1 cm in all three axes. To help aid in visualizing the magnetic fields produced by these individual coils, magnetic field maps at $z = 0.25$ m when the G_x and G_z coils are at the coil strength of 40 mT/m are provided in Figs. 6(c) and 6(d), respectively. As one can see from Fig. 5, there are 27 unique gradient combinations (including the five representative phase-encoding variations) in each sequence. For each of these combinations, 3D vector magnetic fields from each coil are scaled according to the coil strength shown in Figs. 5(a) and 5(b) and are combined into a single magnetic field map file which is used in both the analytic simulations and MC simulations. These combined magnetic fields assume no interaction between the gradient fields and the MRI's magnetic steel structures. As this ignores any potential shielding effect of the yoke on the fringe field of the gradient coils closer to the beam source, it represents a worst-case scenario for effects of gradient fields on the proton trajectory. To investigate the shielding effect of the yoke in this particular design, a combined FEM simulation of gradient fields, the magnetic yoke, and the superconducting coils is included in the study. This combined field simulation was accomplished through an integrated FEM model (using OPERA) in which a model containing the magnetic yoke and superconducting coils was complemented with an array of circular loops approximating the transverse gradient design illustrated in Fig. 6.

The analytic simulations of proton trajectory use the geometric setup shown in Fig. 2. For each θ and ϕ combination, a set of 28 separate analytic simulations is run: one simulation with the magnetic fields from each of the unique gradient combinations in Fig. 5 and one simulation with no magnetic fields present. For each simulation, the proton's 3D track is recorded for analysis. A beam point spread function (PSF) is created for each set of the gradient combinations by weighting each beam with the fraction of time the gradient combination was used in the MR sequence. To fill in the data between the phase encode steps that were used, the cumulative PSF was interpolated to 120 phase encode steps by linearly arranging the beam locations evenly between discrete phase encode steps. The same analytic simulations and analysis are performed for each imaging sequence shown in Figs. 5(a) and 5(b).

The MC simulations use the geometric setup displayed in Fig. 3. Monoenergetic proton pencil beams are used. Each MC simulation uses 10^7 initial protons, and the source of the beam is placed at $z = -130$ cm (Fig. 3). For each θ and ϕ

combination, a set of 28 separate MC simulations is run: one simulation with magnetic fields from each unique gradient combination from Fig. 5 and one simulation with no magnetic fields present. The magnetic fields are applied to the MC simulations by following the same method described in the *Purging Magnet* example. In each simulation, the position of the beam at $z = 0$ cm is recorded. Its surface dose profile is recorded and is weighted according to the segment durations shown in Fig. 5. The cumulative surface dose profile from the set of 27 unique gradient combinations is the sum of the dose of the weighted surface dose profile.

3. RESULTS AND DISCUSSION

The proton source in the current MR imager design is 130 cm away from the center of the MR magnet (Fig. 2). The analytic simulation shows that the proton beam experienced deflections in its trajectories for $\theta > 0^\circ$ (Fig. 7). These deflections, which are caused by the magnetic field components perpendicular to the beam direction, cause the beam to follow a helical path once it is inside the MR magnet. Larger values of θ result in larger deflections as shown in Fig. 7(a) and 7(b). In the fringe field region ($z < -50$ cm), the magnitude of the z-component of the magnetic fields along the central axis (CAX) is small (0.086 T) as shown in Fig. 8(b). A maximum rotation of 0.12°, 0.08°, and 0.06° at $z = -50$ cm was observed for the 80, 150, and 250 proton beams. As the proton beam travels further into the MR magnet ($z > -50$ cm), deflections in beam trajectories start to occur [Fig. 8(a)], which are caused by stronger magnetic field strengths present along the beam path [Fig. 8(b)]. Within the imaging volume of the MR volume ($z = -20$ cm to $z = 20$ cm), the \mathbf{B}_0 field remains homogeneous, and therefore, the increases in the beam deflection are linearly with the z-axis.

The results from the MC simulations that used the vacuum background material agree well with the analytic results. The maximum deviation between the MC results and the analytic results is 0.014 mm at the center of the magnet ($z = 0$ cm) which occurred for the $\theta = 5^\circ$ and $\phi = 90^\circ$ combination.

This second set of MC simulations includes the 20-cm air gap between the vacuum column and the water phantom as shown in Fig. 3. While the effects of the \mathbf{B}_0 field caused an overall shift in the beam's position, the presence of the air gap only caused additional blurring, increasing its FWHM to at most 0.22 mm, without additional shifts in the beam's position. In addition, as illustrated by Figs. 9(a) and 9(b), the shape of the beam's surface dose profile is unaffected by the \mathbf{B}_0 fields. The FWHM for the proton beam with and without the \mathbf{B}_0 fields differed by 0.0004 and 0.005 mm along the x and y direction, respectively. While Fig. 9 only displays the profiles from a 150 MeV monoenergetic proton beam, simulations with 80 and 250 MeV beams show that their surface dose profile is also unaffected by the \mathbf{B}_0 fields. The direction of the beam shown in Figs. 9(a) and 9(b) is $\theta = 6.8^\circ$ and $\phi = 0^\circ$. $\theta = 6.8^\circ$ is the largest angle that was used in this study and places the beam trajectory closest to the edge of the

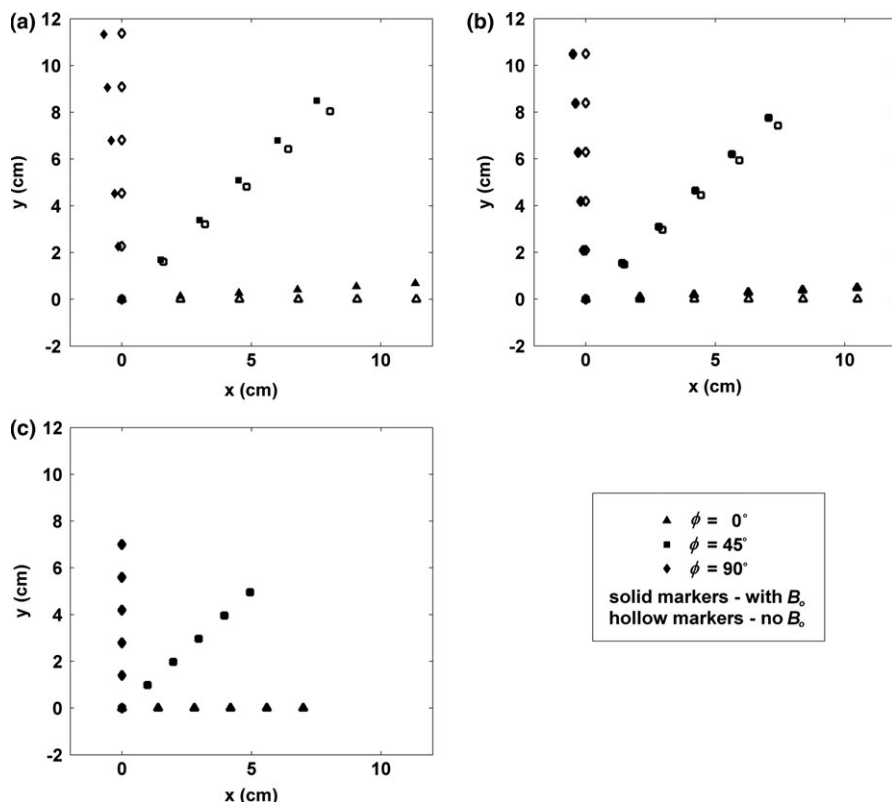


Fig. 7. The xy positions of the 150 MeV proton beam as it passes through three xy plane. For each set of marks, ϕ was kept constant while θ was varied. A beam rotation angle can be calculated when comparing the simulation with and without magnetic fields. For the xy planes (a) $z = 0$ cm plane, the mean rotation angle is 3.479° , (b) $z = -10$ cm plane, this angle is 2.675° , and $z = -50$ cm plane, this angle is 0.084° . The rotation caused by the MR's magnetic fields appears roughly independent of ϕ . Only the positive x and positive y are shown in this graph because of the symmetry of the \mathbf{B}_0 field in the x and y directions.

MR magnet's yoke in the radiation beam portal shown in Fig. 1(b). This set of simulations shows the same rotation calculated from the analytic simulations (Fig. 7). Therefore, beam locations on the phantom surface ($z = 0$ cm) differ by less than 0.0014 mm which is half of the voxel lengths used in the MC simulations.

The proton beam deflections that result from the static \mathbf{B}_0 fields caused the beam to follow a helical trajectory. The behavior of the trajectory is similar to that previously reported¹⁵ although the magnitude of rotation depends on the overall field distribution resulting from the design of the MRI. The magnitude of rotation from our system is substantially lower (by roughly a factor of 4) to that previously reported¹⁵ because of the overall reduced \mathbf{B}_0 field and the reduced fringe fields between the source and the radiation portal (Fig. 1). This design causes the magnetic fields outside of the magnet to rapidly fall from the \mathbf{B}_0 field strength of 0.5 T in the FOV to a fringe magnetic field strength of 0.086 T at $z = -50$ cm which is just outside of the magnet pole to 1.9×10^{-3} T at the exit of the proton nozzle. From Fig. 8(a), the significant beam deflections occur inside the magnet.

3.A. Gradient sequence

To study how the MR's gradient coils affected the proton trajectory, the two variants of the bSSFP sequence

(bSSFP20 and bSSFP40) used are divided into smaller time segments as described earlier and shown in Figs. 5(a) and 5(b), respectively. Cross-sectional maps of the magnetic fields (in Tesla) produced by four gradient combinations from the bSSFP20 sequence are shown in the Fig. 10. Please note greater magnetic field strengths are near the coil regions. These fields are primarily responsible for deflecting the beam on its path toward isocenter. The gradient fields as displayed do not include any effects of field interaction with magnetic yoke structures. These interactions and their effect on proton trajectories will be discussed below.

The time-varying magnetic fields from an MR imaging sequence such as bSSFP40 [Fig. 5(b)] add a blurring effect onto the proton beam. The circles in Figs. 11(a) and 11(b) show the positions of every beam (at the $z = 0$ cm plane) from the 27 separate analytic simulations from the active bSSFP40 sequence. The beam used in Figs. 11(a), 11(c), and 11(e) is a 150 MeV monoenergetic proton pencil beam with initial direction of $\theta = 0^\circ$ and $\phi = 0^\circ$. The initial beam direction used in Figs. 11(c), 11(d), and 11(f) is $\theta = 6.8^\circ$ and $\phi = 45^\circ$, which placed the beam on the outer edge of the MRI's FOV. Figures 11(a) and 11(c) show that there is a good agreement between the analytic and MC results when a vacuum background material is used since the analytic results (the circular markers) overlap with the peaks in the dose deposited in the MC results when the MRI sequence is

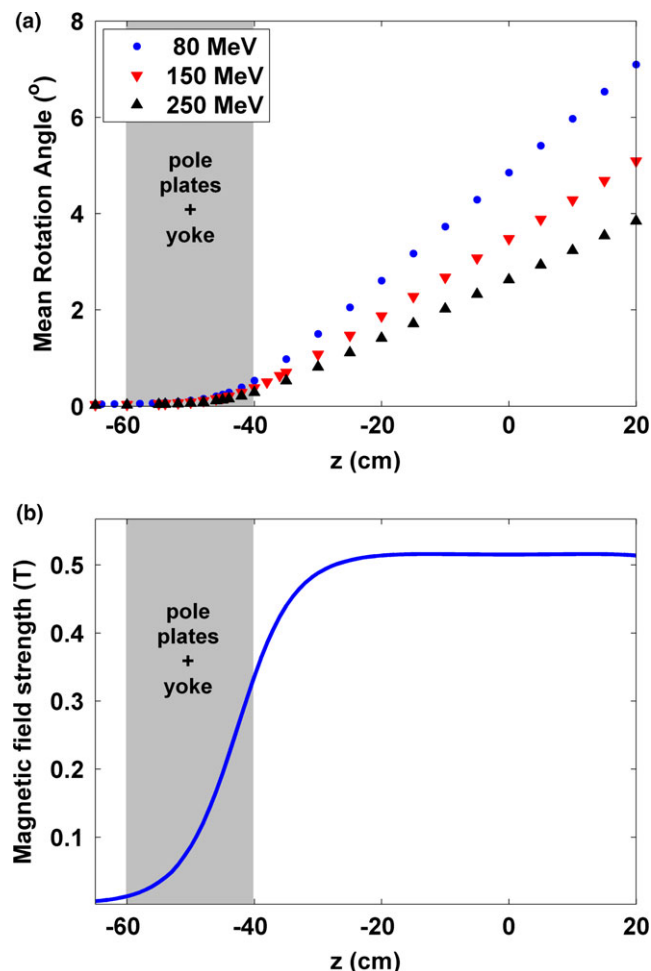


Fig. 8. (a) The average rotation in the proton trajectory as a result of traversing through the MR's magnetic fields. (b) The magnetic field strength in Tesla along the MR's central axis (CAX). [Color figure can be viewed at wileyonlinelibrary.com]

applied to the proton beam. A maximum difference between the positions of the peak doses from the cumulative MC results and the beam positions from the analytic results is less than 0.025 mm. Figure 11(a) shows the pattern in the proton beam's dose distribution that formed when the bSSFP40 sequence was applied to the proton beam: two isolated peak doses from segments A (slice selection) and G (readout) and five sets of peak doses from segments B, C, D, E, and F. The beam distribution along the x-axis reveals the effect of the phase-encoding gradient (in this case G_y). Conversely, the distribution in the y-axis represents the various intensities of the read-encoding gradient throughout the sequence (in this case G_x). The reason for these deflection directions has to do with the perpendicular fields associated with the G_x and G_y coils. While the intent of gradient coils is to produce linear variations of B_z in a particular coordinate axis, there is no way to avoid creating field components perpendicular to \mathbf{B}_0 as well. While these perpendicular fields can often be ignored within an imaging perspective, their existence will lead to deflection of the proton trajectories. The primary perpendicular fields produced by the G_x coil will be oriented in the

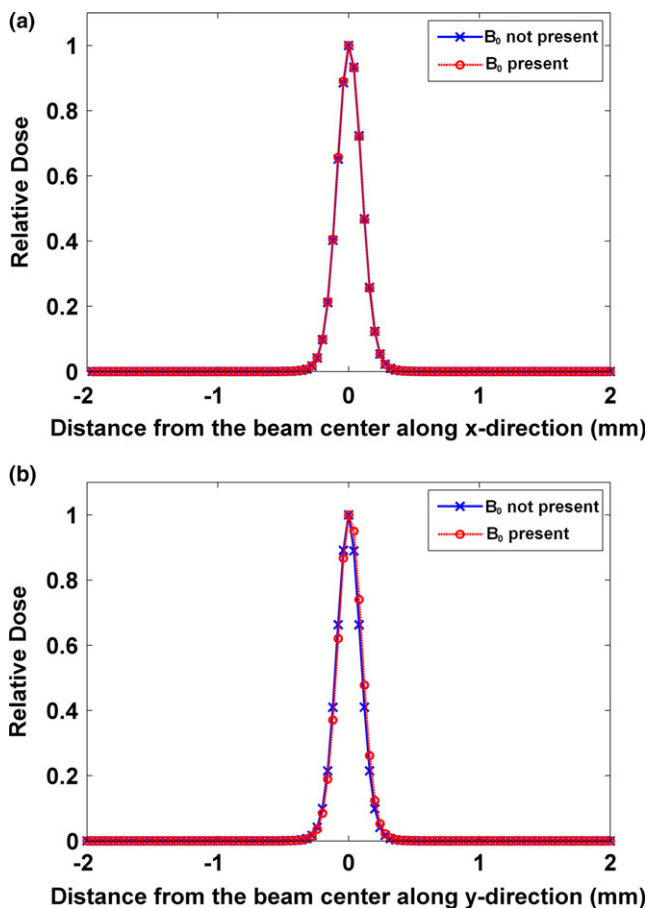


Fig. 9. Profiles of the 150 MeV proton beam's entry dose along (a) the x-axis and (b) the y-axis for $\theta = 6.8^\circ$ and $\phi = 0^\circ$. In both (a) and (b), the blue line (x markers) is the beam profile with the \mathbf{B}_0 field present and the red dotted line (o markers) is the beam profile without the \mathbf{B}_0 field. In all plots, the center of the beam was calculated and used as the center of each profile. These profiles show that although the \mathbf{B}_0 field caused the beam to follow a helical trajectory shape of the surface dose profile of the pencil beam is largely unaffected. The same observation is seen when the beam energy was changed to 80 and 250 MeV. [Color figure can be viewed at wileyonlinelibrary.com]

x-axis, leading to magnetic force and deflection in the y direction, and vice versa for the G_y .⁴² There is no appreciable deflection when the G_z gradient is applied alone without the G_x and G_y gradients (as in the slice selection segment, A), due to minimal perpendicular field components near the central axis in which region the proton beam would predominantly traverse. The results indicate that the deflection in x and y is linearly proportional to the strength of the applied G_y and G_x gradients, respectively.

Figure 11(c) shows the PSF of the beam when the bSSFP40 sequence is used. Without application of any gradients, the PSF would consist of a single spike at the center of the plot. This PSF is created by weighting each beam shown in Fig. 11(a) with the fraction of time its corresponding segment is implemented in the bSSFP40 sequence. To fill in the data between the phase encode steps that were used, the cumulative PSF is interpolated to 120 phase encode steps. The resulting PSF has a spread, which is the difference

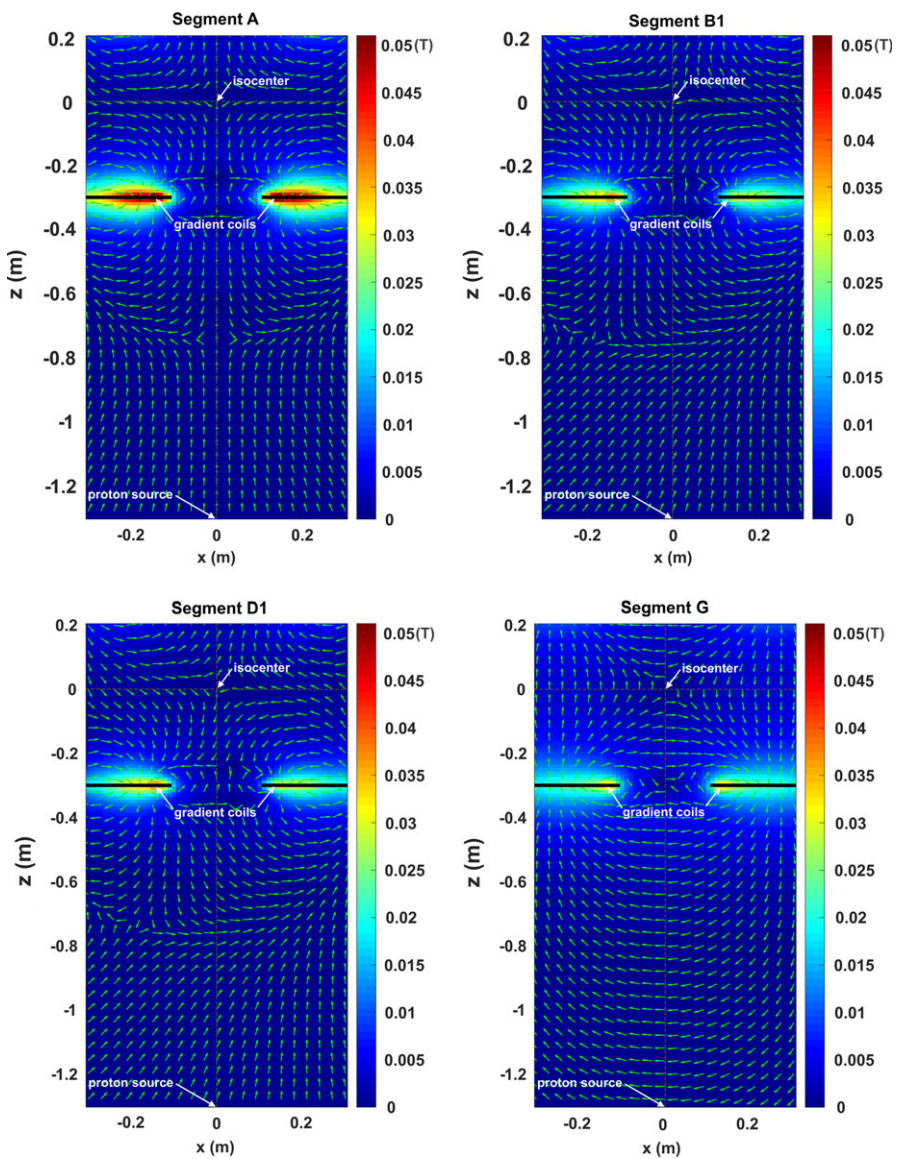


FIG. 10. The cross section of the magnetic field map along the x -axis for segments A (slice selection) (top left), B1 (top right), D1 (bottom left), and G (readout) (bottom right) of the bSSFP20 sequence from Fig. 5(a). The \mathbf{B}_0 field is not included in these field maps. Note that the x direction was chosen only as an example, and due to a lack of rotational symmetry of the transverse gradients, the field patterns would be in general different along the y direction. The color scale in all the field maps shows the magnetic field strength in Tesla (T) while the arrows show its direction. In all the field maps shown, only the gradient coils nearest to the proton source is seen. Note that there are nontrivial perpendicular components in the imaging volume (around $z = 0$). These are generally unimportant to the imaging process but can contribute to beam deflection. [Color figure can be viewed at wileyonlinelibrary.com]

between the minimum and maximum positions in both the x and y direction of 0.5 and 1.1 mm, respectively. The lack of phase encoding during the segments A and G in Fig. 5 results in more defined PSF peaks, accounting for the two prominent peaks in Fig. 11(c). The greater spread in the y direction is caused by the stronger maximum gradient strength used in the G_x coil (40 mT/m) compared to the maximum strength used in the G_y coil (15 mT/m). A change in the beam direction (to $\theta = 6.8^\circ$ and $\phi = 45^\circ$) introduces a small shearing deformation on the pattern seen in Fig. 11(d), since, for $\theta = 6.8^\circ$, the beam passes closer to the gradient coil where the perpendicular components of the magnetic fields are greater resulting in magnetic deflection and deformation of the pattern seen in the $\theta = 0^\circ$ case. This

deformation causes a rotation and a translation for each of the phase encodes used.

When the bSSFP20 sequence [see Fig. 5(a)] is used, the resulting pattern and PSF retain the same shape as described above when the bSSFP40 sequence was used. However, a smaller spread occurs because the weaker maximum gradient strength (20 mT/m) used. At the central plane of the magnet, this spread of the PSF is 0.37 and 0.56 mm in the x and y direction, respectively, for a beam with an initial direction of $\theta = 0^\circ$ and $\phi = 0^\circ$. The pattern and PSF for this beam are shown in Figs. 12(a) and 12(c), respectively. Figures 12(b) and 12(d) show similar shearing deformation in the pattern and PSF seen in the bSSFP cases when the beam direction is changed to

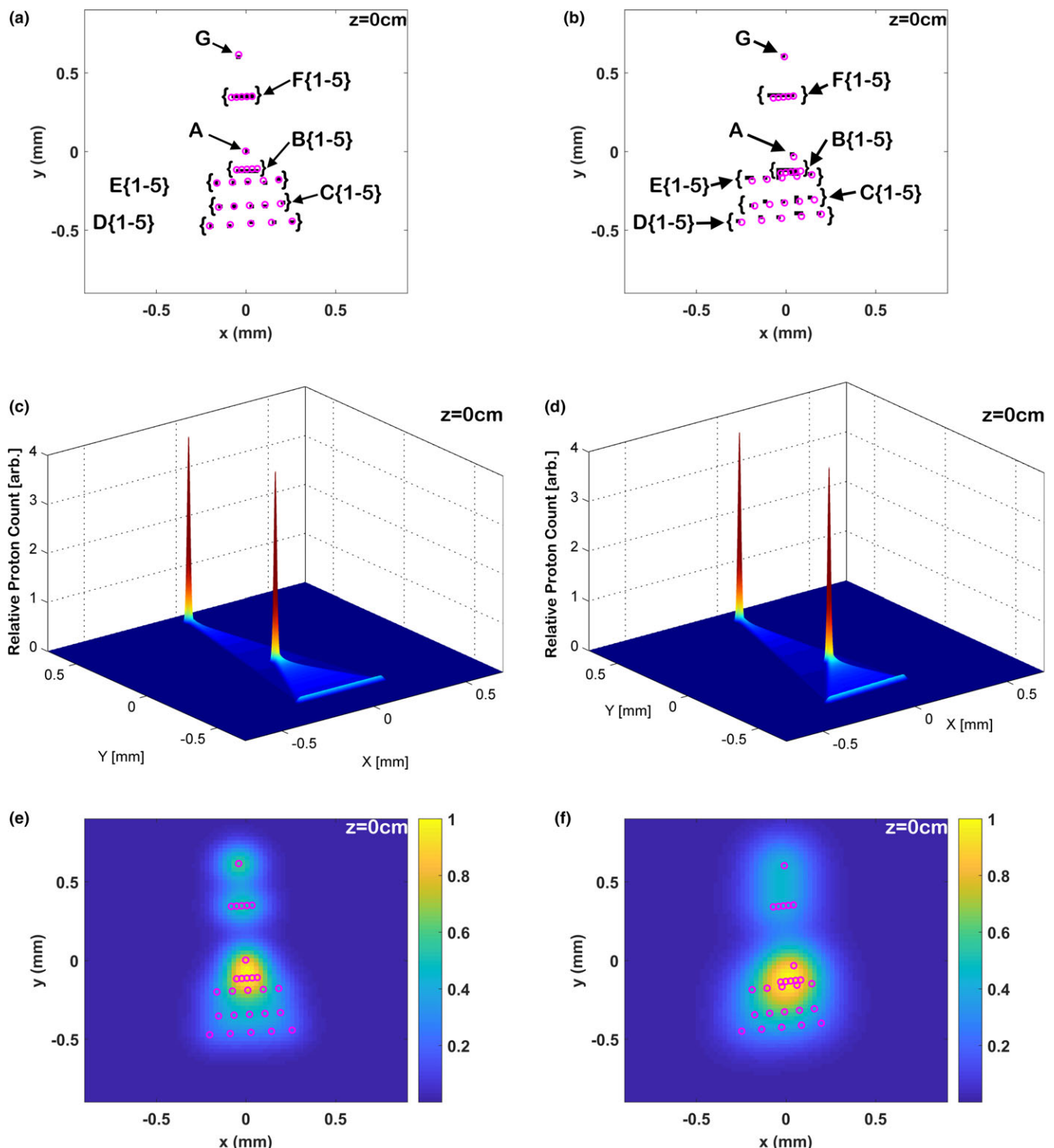


FIG. 11. The resulting pattern in (a) and (b) shows the location of the beam at the phantom surface ($z = 0 \text{ cm}$). The beam in (a) has an initial direction that coincides with the z -axis ($\theta = 0^\circ$ and $\phi = 0^\circ$), while the beam's initial direction in (b) is $\theta = 6.8^\circ$ and $\phi = 45^\circ$. The analytic results (circles) show good agreement with and are superimposed on the Monte Carlo results. The graphs in (c) and (d) are the point spread functions for (a) and (b), respectively. (e) and (f) show the effect of the addition of a 20 cm air gap between vacuum column and phantom surface (see Fig. 3). All simulations applied the magnetic fields from the bSSFP40 sequence to a 150 MeV proton pencil beam. The labels A (slice selection) to G (readout) refer to the different segment of the bSSFP40 sequence from Fig. 5(b) while the numbers 1–5 refer to the five phase encodes used during the simulations. [Color figure can be viewed at wileyonlinelibrary.com]

$\theta = 6.8^\circ$ and $\phi = 45^\circ$. The presence of the MR's \mathbf{B}_0 fields causes a rotation of each beam in the pattern around the z -axis. Its effects are independent of the blurring effect caused by the gradient fields.

Varying the energy of the proton beam affects the extent of the spread in the pattern observed in Figs. 11 and 12. For an 80 MeV proton beam, this spread in the x and y direction is 0.51 and 0.77 mm when the bSSFP20 sequence was used.

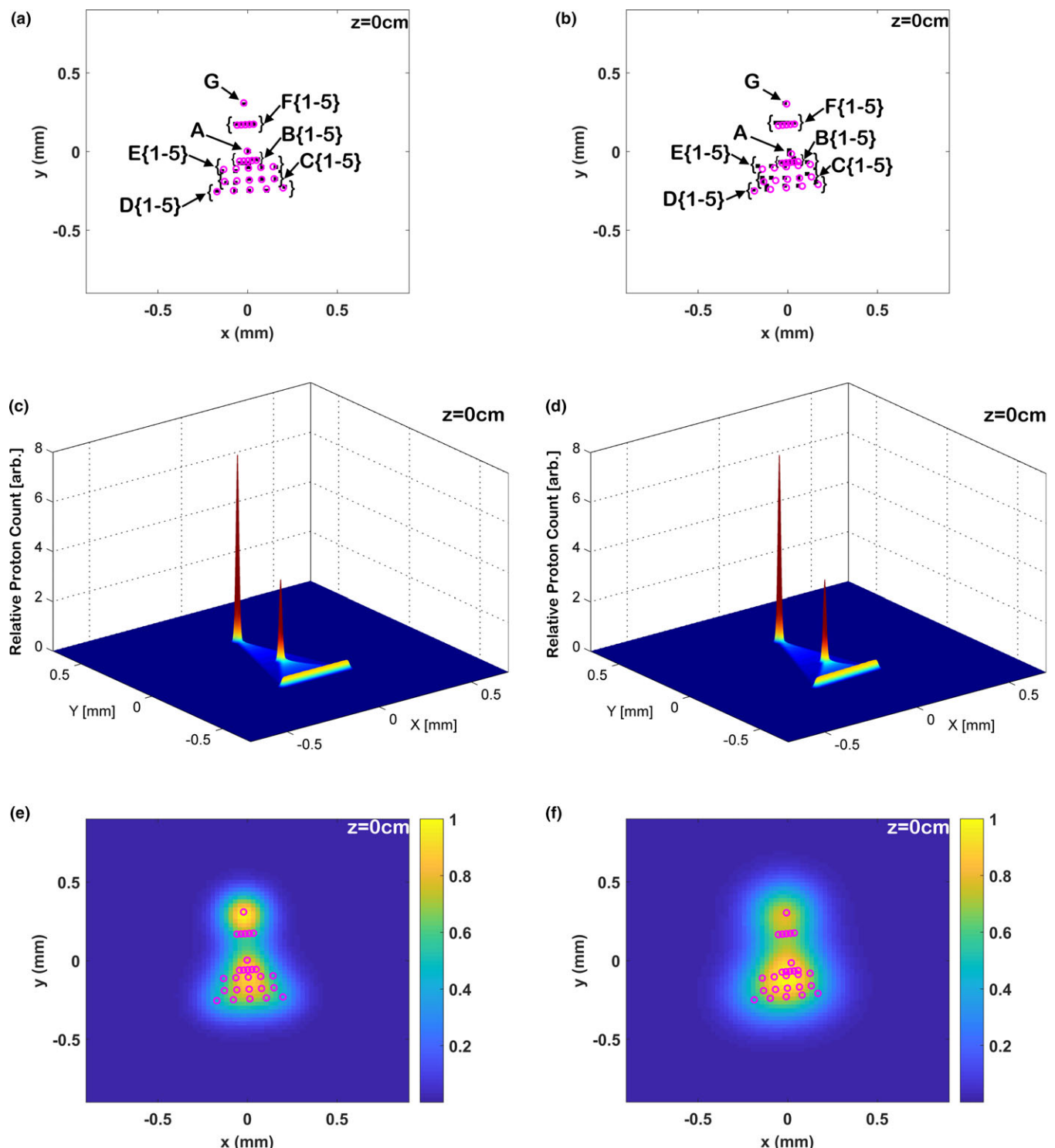


FIG. 12. The resulting pattern in (a) and (b) shows the location of the beam at the phantom surface ($z = 0\text{ cm}$). The beam in (a) has an initial direction that coincides with the z -axis ($\theta = 0^\circ$ and $\phi = 0^\circ$), while the beam's initial direction in (b) is $\theta = 6.8^\circ$ and $\phi = 45^\circ$. The analytic results (circles) show good agreement with and are superimposed on the Monte Carlo results. The graphs in (c) and (d) are the point spread functions for (a) and (b), respectively. (e) and (f) show the effect of the addition of a 20 cm air gap between vacuum column and phantom surface (see Fig. 3). All simulations applied the magnetic fields from the bSSFP20 sequence to a 150 MeV proton pencil beam. The labels A (slice selection) to G (readout) refer to the different segment of the bSSFP20 sequence schematic from Fig. 5(a) while the numbers 1–5 refer to the five phase encodes during in the simulations. [Color figure can be viewed at wileyonlinelibrary.com]

It is 0.64 and 1.5 mm when the bSSFP40 sequence was used. For the 250 MeV proton beam, the spread is reduced to 0.28 and 0.41 mm in the x and y direction for the bSSFP20

sequence; it is 0.35 and 0.82 mm in the x and y direction for the bSSFP40 sequence. The shape of this pattern and the PSF are unaffected when the energy of the beam was varied.

3.B. The effects of the MRI's ferromagnetic structures

The results presented in Figs. 11 and 12 ignored any potential shielding effect on the gradient fields due to steel structural components of the MRI, and as such represent a worst-case scenario of proton deflection in a parallel configured hybrid system. However, the particular design evaluated in this study has a considerable mass of magnetic steel between the proton source and the gradient coils, shown in Fig. 1(b), which combined FEM simulations have shown to impact the gradient field distribution and resulting proton trajectory, displayed in Fig. 13. Here, a reduction in field is seen between the gradient-coil current loops and the proton source. While the reduction in the field is of low magnitude [see Fig. 13(d)], the extent of this small change over a large

fraction of the proton path has a marked effect on the position of the beam at MRI isocenter. In addition to a $\sim 1/3$ reduction in the magnitude of deflection at isocenter, Fig. 13(a) shows a reversal of this deflection polarity due to the loss of the initial transverse fields closer to the proton source which is oriented opposite to the transverse fields at the entrance to the imaging field of view. This effect would naturally affect (and reduce) the patterns illustrated in Figs. 11 and 12. However, unlike the effects shown in Figs. 11 and 12, this effect will be dependent on magnet design and yoke.

The nature of the beam distribution as illustrated in this work may be deemed as tolerable in a treatment scenario. However, should it be desired that this added uncertainty be avoided, there are options for eliminating this contribution. Firstly, as has been suggested for deflections due to \mathbf{B}_0 , the effects of the time-varying gradients could be calibrated and

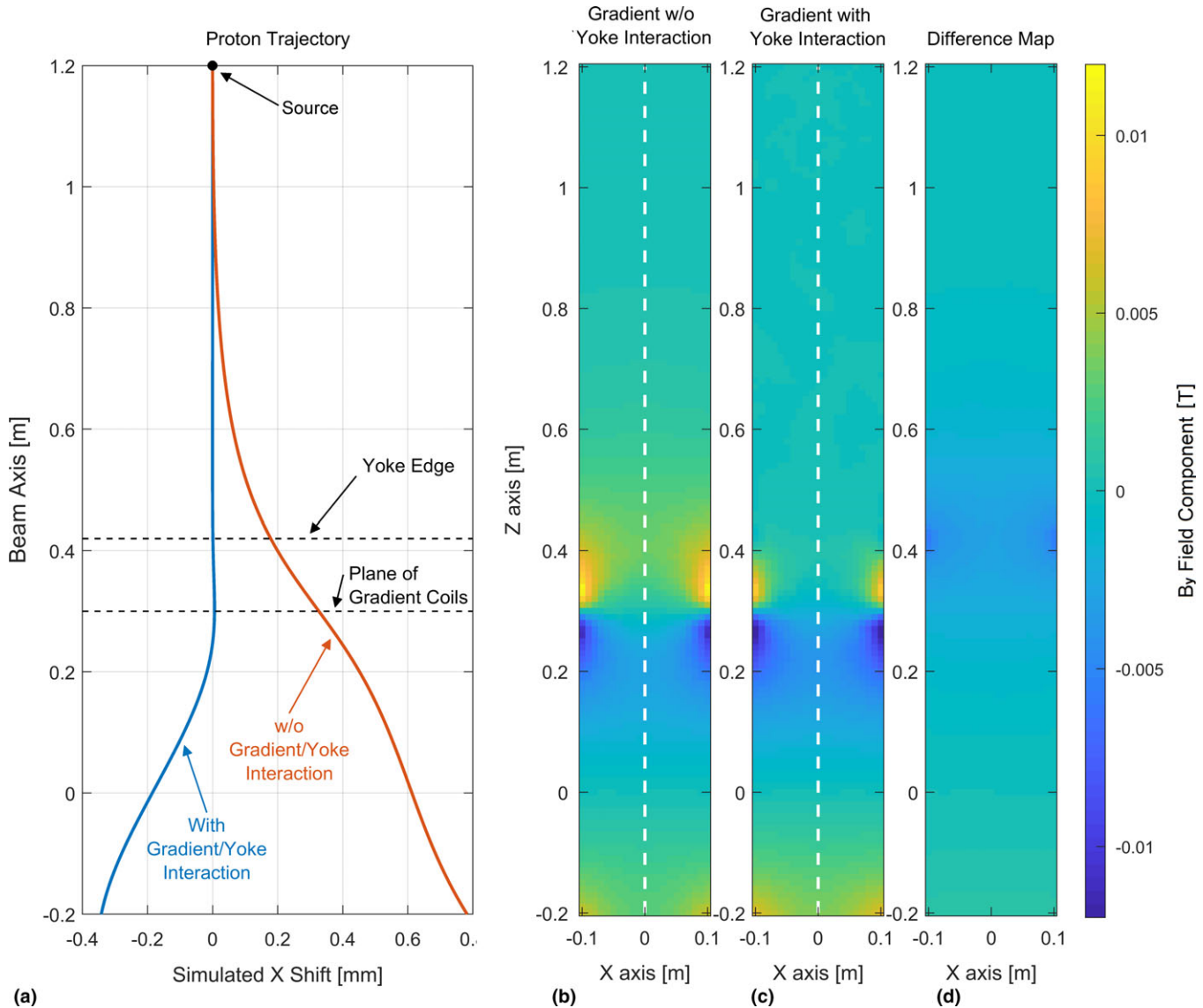


FIG. 13. The effect of the magnetic structures in the yoke of the magnet design studied in this work on the fringe field of gradient coil sets and the consequence on proton trajectory. (a) 80 MeV proton trajectories on axis with and without the shielding effect of the yoke. (b) B_y component of a transverse gradient coil set without magnetic shielding of the yoke and (c) with the magnetic shielding of the yoke. (d) Difference map between the field maps of (b) and (c). [Color figure can be viewed at wileyonlinelibrary.com]

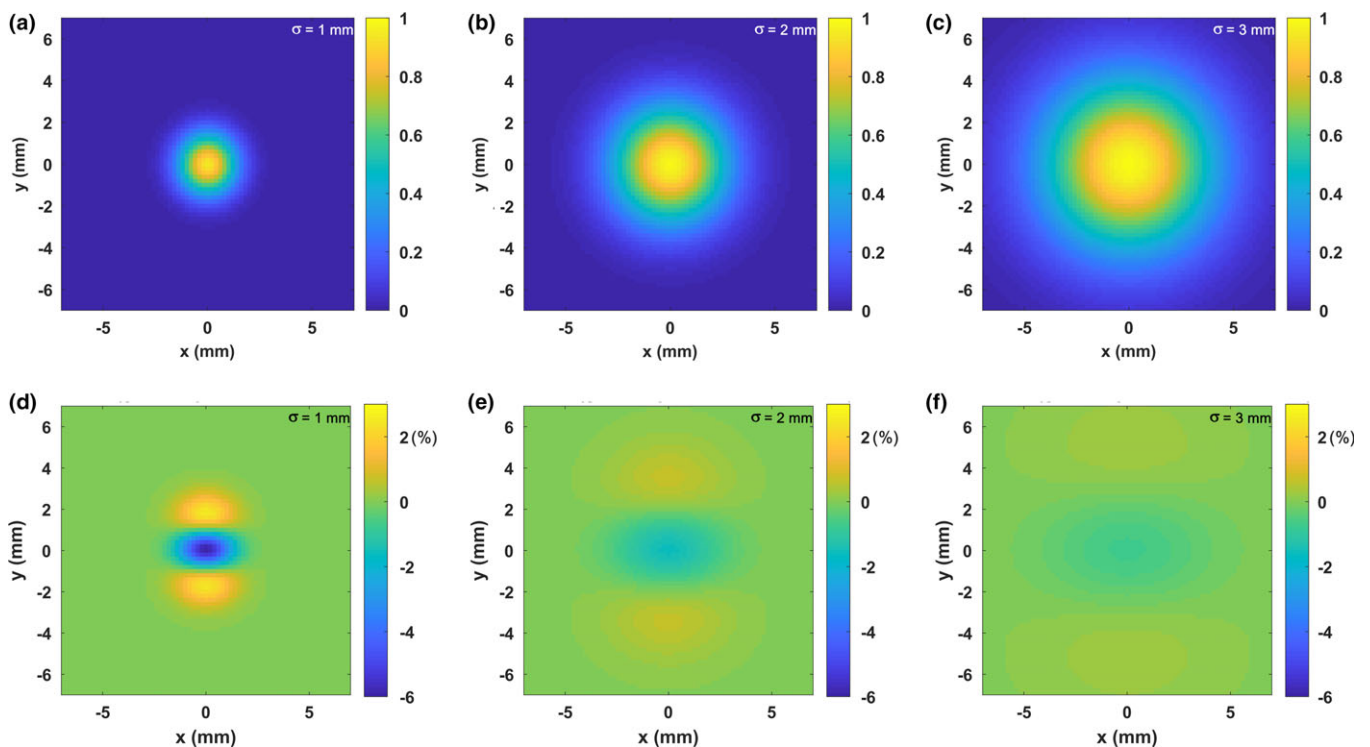


FIG. 14. (a), (b), and (c) show the results of the convolution between the pattern in Fig. 11(a) and a beam with a Gaussian density distribution with varying σ (1, 2, and 3 mm, respectively). The percent difference maps between dose profiles with and without the bSSFP40 sequence active are shown (d), (e), and (f) for each σ used. [Color figure can be viewed at wileyonlinelibrary.com]

compensated for in real time. This corrective method requires precise timing between the activation of the gradients and the correction of the beam direction. Therefore, this method may require additional controls mechanism. Alternatively, an interlacing strategy could be implemented to beam on and acquire imaging data at alternating times, removing the added blur, albeit at an expense of efficiency. The radio frequency (RF) pulses that are used in MRI for excitation also produce time-varying magnetic fields. These fields are usually in the order of μT in contrast to gradient fields which are in the order of mT .⁴³ Hence, it is expected that these fields would produce blurring effects three orders of magnitude smaller than those predicted here.

3.C. Extensions to proton pencil beams with finite width

This study isolated and quantified the effects of the time-varying magnetic fields from the gradient coils on the proton beam. Infinitely, thin pencil beam source was used to accomplished this goal and show that gradient coils' magnetic fields during an MRI imaging sequence created the pattern shown in Figs. 11 and 12. However, beam sources from clinical PBS have finite width. Assuming that a circular pencil beam spot, with a Gaussian distribution profile, was used, the beam width can be characterized by the standard deviation σ . The FWHM is equal to 2.35σ . Factors such as treatment time, treatment sites, delivery uncertainties, and machine capabilities are used to determine the appropriate value of σ . The PSF and the 2D dose profiles featured in Figs. 11 and 12

would need to be convolved over this realistic pencil beam to determine the overall effect on dose deposition when the MRI sequence is used concurrently with the proton beam. Assuming that the protons have parallel trajectories at the source because of the beam's low emittance ($\sim 1 \pi$ mm mrad),⁴⁴ Figs. 14(a)–14(c) show the results of convolving the pattern seen in Fig. 11(a) with beams with $\sigma = 1$, 2, and 3 mm. The pattern from Fig. 11(a) can no longer be seen. The percent difference maps between the dose profiles with and without the bSSFP40 sequence active [Figs. 14(d)–14(f)] show that the effects of the gradient fields become less significant with increasing beam width, where the largest maximum hot spot (3%) and cold spot (6%) occurred when the smallest σ (1 mm) was used. The magnitude of the maximum hot spot and cold spot decreased to 0.3 % and 0.7 %, respectively, when the largest σ (3 mm) was studied as shown Fig. 14(f). Therefore, an active MRI sequence would have an insignificant impact of the beam's entrance dose.

The Alberta setup was used because it is a compact system which have both the MRI and linac mounted directly onto the same rotating gantry, which ensures that the MRI and linac rotate in unison. In proton systems with rotating gantries,³⁴ the proton nozzle, along with the scanning magnets, and beam transport magnets would rotate along with the gantry. Although some mechanical redesign of the gantry would be required, the proton nozzle assembly and the rotating portion of the beam line can be mounted onto the same rotating gantry as the MRI. Although simulations shown that the current gantry/steel yoke design provide some magnetic shielding, additional magnetic shielding may be necessary to

completely decouple the MRI from the proton assembly's stirring magnets and the XY scanning magnets.

4. CONCLUSION

The effects of realistic MRI magnetic fields from two different sources (the main magnet and the gradient coils) on monoenergetic proton pencil beams were studied by computer simulations for a hybrid device based on the Alberta 0.5 T rotating biplanar MR radiotherapy design in the parallel configuration. The results of the analytic simulations agreed well with the MC results, differing by less than 0.025 mm at the center of the magnet. Both sources of magnetic fields caused deflections in the proton beam trajectories. In the presence of the static \mathbf{B}_0 fields, the proton beams studied followed a helical path through the imaging volume with average angular rotation at the center of the magnet of 4.9°, 3.6°, and 2.8° for the 80, 150, and 250 MeV monoenergetic proton beams studied, respectively. The beam rotations observed in this work can become an issue for consideration near the outer edge of the MRI's FOV where the proton beam deflections are amplified. This effect is dependent on the design of the imager and will be static. A solution to resolve this effect is to precalculate the proton beam's trajectory and adjust its source direction accordingly.

The magnetic deflections in the beam trajectories caused by gradient coils' magnetic fields resulted in a blurring effect applied to the PSF of the proton pencil beams used in this investigation. For an 80 MeV beam, the spread in the PSF was 1.5 mm for the bSSFP40 and 0.77 mm for bSSFP20. Our results indicated that the amount of spread seen in the PSF due to the use of imaging gradients will be linearly dependent on the maximum intensity of the G_x and G_y gradient fields required by a sequence. However, results also show that the extent of these deflections can be greatly reduced by the shielding effects of the MR's steel structures on the gradient coil fields outside the imaging volume. In addition, the difference maps in Fig. 14 show the impact of the gradient fields on the clinical beam's entrance dose become less significant the wider the beam. Therefore, for a common clinical beam width ($\sigma = 3$ mm), the gradient fields are expected to have no clinical dosimetry implications for MR imaging sequence and proton MRI setup that was studied.

CONFLICTS OF INTEREST

Dr. Fallone is a cofounder and CEO of MagnetTx Oncology Solutions, Ltd. (PO Box 52112) in Edmonton, AB, Canada.

^{a)}Author to whom correspondence should be addressed. Electronic mail: dsantos@ualberta.ca

REFERENCES

1. Fallone BG, Stanescu T, Steciw S, Vidakovic S, Blosser E, Tymofichuk D. First MR images obtained during megavoltage photon irradiation from a prototype integrated linac-MR system. *Med Phys.* 2009;36: 2084–2088.
2. Raaymakers BW, Lagendijk JJW, Overweg J, et al. Integrating a 1.5 T MRI scanner with a 6 MV accelerator: proof of concept. *Phys Med Biol.* 2009;54:N229–N237.
3. Green OL, Hu Y, Noel C, Olsen JR, Mutic S. Observation of radiation-induced tissue signal intensity changes with the first commercial MRI-guided IMRT system. *Int J Radiat Oncol Biol Phys.* 2012;84:S758–S759.
4. Liney GP, Dong B, Weber E, et al. Imaging performance of a dedicated radiation transparent RF coil on a 1.0 Tesla inline MRI-linac. *Phys Med Biol.* 2018;63:135005.
5. Constantin DE, Fahrig R, Keall PJ. A study of the effect of in-line and perpendicular magnetic fields on beam characteristics of electron guns in medical linear accelerators. *Med Phys.* 2011;38:4174–4185.
6. Santos DM, St Aubin J, Fallone BG, Steciw S. Magnetic shielding investigation for a 6 MV in-line linac within the parallel configuration of a linac-MR system. *Med Phys.* 2012;39:788–797.
7. Kok JGM, Raaymakers BW, Lagendijk JJW, Overweg J, de Graaff CHW, Brown KJ. Installation of the 1.5 T MRI accelerator next to clinical accelerators: impact of the fringe field. *Phys Med Biol.* 2009;54:N409–N415.
8. St. Aubin J, Steciw S, Fallone BG. Magnetic decoupling of the linac in a low field biplanar linac-MR system. *Med Phys.* 2010;37:4755–4761. <https://doi.org/10.1111/1.3480482>
9. Crijns SPM, Bakker CJG, Seevinck PR, de Leeuw H, Lagendijk JJW, Raaymakers BW. Towards inherently distortion-free MR images for image-guided radiotherapy on an MRI accelerator. *Phys Med Biol.* 2012;57:1349–1358.
10. Lamey M, Rathee S, Johnson L, Carbone M, Blosser E, Fallone BG. Radio frequency noise from the modulator of a linac. *IEEE Trans Electromagn Compat.* 2010;52:530–536.
11. Lamey M, Burke B, Blosser E, Rathee S, De Zanche N, Fallone BG. Radio frequency shielding for a linac-MRI system. *Phys Med Biol.* 2010;55:995–1006.
12. Tadic T, Fallone BG. Design and optimization of superconducting MRI magnet systems with magnetic materials. *IEEE Trans Appl Supercond.* 2012;22:4400107.
13. Raaymakers BW, Raaijmakers AJE, Lagendijk JJW. Feasibility of MRI guided proton therapy: magnetic field dose effects. *Phys Med Biol.* 2008;53:5615–5622.
14. Moteabbed M, Schuemann J, Paganetti H. Dosimetric feasibility of real-time MRI-guided proton therapy. *Med Phys.* 2014;41:111713.
15. Oborn BM, Dowdell S, Metcalfe PE, Crozier S, Mohan R, Keall PJ. Proton beam deflection in MRI fields: implications for MRI-guided proton therapy. *Med Phys.* 2015;42:2113–2124.
16. Kurz C, Landry G, Resch AF, et al. A monte-carlo study to assess the effect of 1.5 T magnetic fields on the overall robustness of pencil-beam scanning proton radiotherapy plans for prostate cancer. *Phys Med Biol.* 2017;62:8470.
17. Maspero M, van den Berg CAT, Landry G, et al. Feasibility of MR-only proton dose calculations for prostate cancer radiotherapy using a commercial pseudo-CT generation method. *Phys Med Biol.* 2017;62:9159.
18. Bradley Oborn BM, Dowdell S, Metcalfe PE, Crozier S, Mohan R, Keall PJ. Future of medical physics: real-time MRI-guided proton therapy. *Med Phys.* 2017;44:e77–e90.
19. Shao W, Tang X, Bai Y, et al. Modulation of lateral positions of Bragg peaks via magnetic fields inside cancer patients: toward magnetic field modulated proton therapy. *Med Phys.* 2017;44:5325–5338.
20. Schellhammer SM, Sebastian G, Armin L, Oborn BM, Bussmann M, Hoffmann AL. Technical note: experimental verification of magnetic field-induced beam deflection and Bragg peak displacement for MR-integrated proton therapy. *Med Phys.* 2018;45:3429–3434.
21. Schellhammer S, Karsch L, Smeets J, et al. First in-beam MR scanner for image-guided proton therapy: beam alignment and magnetic field effects. *Radiother Oncol.* 2018;127:S318–S319.
22. Schellhammer SM, Hoffmann AL. Prediction and compensation of magnetic beam deflection in MR-integrated proton therapy: a method optimized regarding accuracy, versatility and speed. *Phys Med Biol.* 2017;62:1548–1564.
23. Fuchs H, Moser P, Groschl M, Georg D. Magnetic field effects on particle beams and their implications for dose calculation in MR-guided particle therapy. *Med Phys.* 2017;44:1149–1156.

24. Fatima P-C, Dietmar G, Fuchs H. A pencil beam algorithm for magnetic resonance image guided proton therapy. *Med Phys.* 2018;45:2195–2204.
25. Dale BM, Brown MA, Semelka RC. *MRI: Basic Principles and Applications*, 5th ed. Hoboken, NJ: John Wiley & Sons Ltd.; 2015.
26. Keyvanloo A, Burke B, St.Aubin J, et al. Minimal skin dose increase in longitudinal rotating biplanar linac-MR systems: examination of radiation energy and flattening filter design. *Phys Med Biol.* 2016;61:3527–3539.
27. Fallone BG. The rotating biplanar linac-magnetic resonance imaging system. *Semin Radiat Oncol.* 2014;24:200–202.
28. Keyvanloo A, Burke B, Warkentin B, et al. Skin dose in longitudinal and transverse linac-MRIs using Monte Carlo and realistic 3D MRI field models. *Med Phys.* 2012;39:6509–6521.
29. Anferov V. Combined X—Y scanning magnet for conformal proton radiation therapy. *Med Phys.* 2015;32:815–818.
30. Lau A, Chen Y, Ahmad S. Yields of positron and positron emitting nuclei for proton and carbon ion radiation therapy: a simulation study with GEANT4. *J Xray Sci Technol.* 2012;20:317–329.
31. Anferov VA. Scan patter optimization for uniform proton beam scanning. *Med Phys.* 2009;36:3560–3567.
32. Jelen U, Bubula ME, Ammazzalorso F, Engenhart-Cabillic R, Weber U, Wittig A. Dosimetric impact of reduced nozzle-to-isocenter distance in intensity-modulated proton therapy of intracranial tumors in combined proton-carbon fixed-nozzle treatment facilities. *Radiat Oncol.* 2013;8:218.
33. Widesott L, Lomax AJ, Schwarz M. Is there a single spot size and grid for intensity modulated proton therapy? Simulation of head and neck, prostate and mesothelioma cases. *Med Phys.* 2012;39:1298–1308.
34. Liu X, Qin B, Liu K, Chen W, Liang Z, Chen Q. Design of the fast scanning magnet for HUST Proton Therapy Facility. In: 21st International Conference on Cyclotrons and their Applications. Zurich, Switzerland: Paul Scherrer Institut; 2016:42–44.
35. Arduini G, Cambria R, Canzi C, et al. Physical specifications of clinical proton beams from a synchrotron. *Med Phys.* 1996;23:939–951.
36. Wolf R, Bortfeld T. An analytical solution to proton Bragg peak deflection in a magnetic field. *Phys Med Biol.* 2012;57:N329–N337.
37. Hartman J, Kontaxis C, Bol GH, et al. Dosimetric feasibility of intensity modulated proton therapy in a transverse magnetic field of 1.5 T. *Phys Med Biol.* 2015;60:5955–5969.
38. Allison J, Amako K, Apostolakis J, et al. Geant4 developments and applications. *IEEE Trans Nucl Sci.* 2006;53:270–278.
39. Brown RW, Cheng YC, Haacke EM, Thompson MR, Venkatesan R. Fast imaging in the steady state. In: *Magnetic Resonance Imaging: Physical Principles and Sequence Design*, 2nd ed. Hoboken, NJ: John Wiley & Sons Inc.; 2014:447–510.
40. Lemdiasov RA, Ludwig R. A stream function method for gradient coil design. *Concepts Magn Reson.* 2005;26B:67–80.
41. Poole M, Bowtell R. Novel gradient coils designed using a boundary element method. *Concepts Magn Reson.* 2007;31B:162–175.
42. Norris DG, Hutchison JM. Concomitant magnetic field gradients and their effects on imaging at low magnetic field strengths. *Magn Reson Imaging.* 1990;8:33–37.
43. Nishimura DG. *Principles of Magnetic Resonance Imaging*. Standford, CA: Stanford University; 1996:34–37.
44. Variale V, Mastromarco M, Colamaria F, Colella D. New beam scanning device for active beam delivery system (BDS) in proton therapy. *Phys Procedia.* 2017;90:223–228.